Mass-profile quantum dots in graphene and artificial periodic structures

A. Gutiérrez-Rubio and T. Stauber

Departamento de Teoría y Simulación de Materiales, Instituto de Ciencia de Materiales de Madrid, CSIC, E-28049 Madrid, Spain

(Received 26 November 2014; revised manuscript received 4 February 2015; published 14 April 2015)

We analyze the bound-state spectra of mass-profile quantum dots in graphene, a system at current experimental reach. Homogeneous perpendicular magnetic fields are also considered which result in breaking the valley degeneracy. The spectra show rich features, arising from the chiral band structure of graphene and its Landau levels and we identify three different regimes depending on the ratio between the radius of the dot and the magnetic length. We further carry out a comparison with potential-well quantum dots discussed in Recher *et al.* [Phys. Rev. B **79**, 085407 (2009)] and conclude that mass confinement may offer significant advantages for optical applications in the THz and infrared regime. Also due to experimental advances, we additionally analyze the band structure of a linear chain of mass-profile quantum dots, where overlap-assisted hopping processes play a major role for closely packed arrays. The inclusion of Coulomb interactions between electron-hole pairs of adjacent sites leads to a new regime where Förster transfer processes become dominant.

DOI: 10.1103/PhysRevB.91.165415 PACS number(s): 81.07.Ta

I. INTRODUCTION

Due to the chiral nature of its carriers, gapless graphene cannot confine electrons via a lateral electrostatic potential [1,2]. Several setups have been found to tackle this problem, producing nanostructures of graphene in form of quantum dots [3,4] or nanoribbons [5,6]. Moreover, confining Dirac electrons in rings with edge reconstruction [7–9], inhomogeneous constant magnetic fields [10–12], superlattices over different substrates [13–15] with a modulated Fermi velocity [16] or scalar potential [17], as well as nanohole patterning [18] and topological mass terms [19–22] have been discussed. Achieving this gap opening is essential in regard to the design of nanodevices or possible applications to quantum computing [23,24].

Once we count on the possibility of opening a gap and confining electronic states, the ability to control the level degeneracy is of high interest. As an example, valleytronic devices [25] or spin qubits [24,26] usually require a lifted valley degeneracy to be engineered, although some alternatives have been proposed recently [27]. This, in turn, is achievable by means of magnetic fields [7,28] or etching graphene ribbons with armchair boundaries [24].

In this paper, we study yet another alternative to confine electrons in graphene consisting in a position-dependent gap. This possibility was first discussed in the context of infinite-mass boundaries by Berry and Mondragon and was mainly motivated by theoretical considerations [29]. Other works have also analyzed the spectra of circularly shaped finite-mass profiles in the presence of electromagnetic fields [30–32]. Here our renewed interest is based on recent experiments on graphene on top of an Ir(111) substrate covered by iridium clusters. Covered and uncovered regions show different particle gaps, but the substrate and the clusters leave graphene's linear spectrum almost unaffected [13]. Quantum dots confined by a finite mass-boundary thus can be designed with nanosize accuracy where the local change in the one-particle gap is introduced by the removal of substrate clusters selected at will by a scanning tunneling microscope (STM) tip [33]. So different quantum dot sizes and geometries are within reach and shall be discussed here.

In particular, we will study the bound-state spectrum of a circular dot as a function of the radius and the magnetic field dependence. We will further establish a comparison between our system, i.e., mass-profile quantum dots (MP-QDs), and a potential-well quantum dot (PW-QD) previously characterized in Refs. [28,34]. We discuss their similar dependence on the dot size and the magnetic field and that the valley degeneracy splits proportionally to B in both cases. On the other hand, we note several differences between them, e.g., the spectrum of MP-QDs being particle-hole symmetric and less dense, thus being more susceptible to optical experiments. Dealing with a simpler level structure may be advantageous also for applications, which endorses the interest in featuring MP-QDs. Finally, we relate the properties of the spectra obtained at high B fields to the nontrivial Berry phase of π in graphene. This gives rise to striking differences with respect to quantum dots hosted by other systems like a conventional two-dimensional (2D) electron gas. We emphasize the novelty of this regime, which has not been addressed in the aforementioned related works and might be at experimental reach also in systems with high local strains [35].

At last, again due to the experimental feasibility to create periodic arrays of identical nanostructures and in regard to possible applications like those introduced in Ref. [36], a linear chain of MP-QDs is analyzed. Its band structure is calculated for a fixed radius R as a function of the lattice parameter D, and the relevance of overlap-assisted hopping processes is discussed for closely packed arrays. Single-particle processes such as hopping or spontaneous decay rates are compared to excitonic processes. Varying the distance between the dots allows us to tune to a Frenkel excitonic regime which can be described by a bosonic tight-binding Hamiltonian.

The paper is organized as follows. In Sec. II, we present the model for mass-profile quantum dots and its solution. In Sec. III A, we discuss the spectrum at $B = 0$ for MP-QDs and PW-QDs, whereas in Sec. III B we extend this analysis to $B \neq 0$. Section IV A focuses on a MP-QD one-dimensional linear chain, and in Sec. IV B the Coulomb interaction between electrons is included. We summarize our conclusions in Sec. V.

In three appendices, we present details of the solution of the eigenvalue problem and define the tight-binding model for arbitrary arrays of MP-QDs.

II. THE MODEL

We shall consider graphene with a position-dependent gap $2\Delta(r)$. The Hamiltonian can be written as

$$H_\tau = H_0 + \tau\Delta(r)\sigma_z, \tag{1}$$

with

$$H_0 = v_F(\vec{p} + e\vec{A})\cdot\vec{\sigma}, \tag{2}$$

$$\vec{B} = \nabla\times\vec{A} = (0,0,B), \tag{3}$$

where $\vec{\sigma} = (\sigma_x,\sigma_y)$ and σ_z are the Pauli matrices, $v_F = 10^6$ m/s is the Fermi velocity, $e > 0$, and the index $\tau = \pm 1$ labels the valleys.

The mass profile is considered to be circularly symmetric and steplike, $\Delta(r) = m_1 v_F^2\Theta(r-R) + m_2 v_F^2\Theta(R-r)$, where R is the radius of the quantum dot. It can be solved by exploiting the rotational invariance, $[J_z, H_\tau] = 0$, with $J_z = -i\partial_\phi + \sigma_z/2$ the total angular momentum—orbital plus lattice—projected onto the $\hat{z}$ direction. So in polar coordinates, the eigenvectors can be written as

$$\psi^\tau(r,\phi) = e^{i(j-1/2)\phi}\begin{bmatrix}\chi_A^\tau(r)\\ \chi_B^\tau(r)e^{i\phi}\end{bmatrix}, \tag{4}$$

where j is a half-odd integer. With Eq. (4), the eigenvalue problem of the Hamiltonian, Eq. (1), can be written as

$$r^2\partial_r^2\chi_\sigma^\tau(r) + r\,\partial_r\chi_\sigma^\tau(r) = \left(b^2r^4 + a_\sigma r^2 + n_\sigma^2\right)\chi_\sigma^\tau(r), \tag{5}$$

where $\sigma = \pm 1$ corresponds to the A/B sublattice. We have also defined

$$a_\sigma = 2b(j+\sigma/2) - (E^2-\Delta^2)/(\hbar v_F)^2, \tag{6}$$

$$\Delta = mv_F^2\,,\quad n_\sigma = |j-\sigma/2|\,,\quad b = \frac{eB}{2\hbar}. \tag{7}$$

The solutions of Eq. (5) are given in Appendices A and B for nonzero magnetic field $B \neq 0$ and $B = 0$, respectively. The matching conditions imposed on Eq. (4) at $r = R$, also detailed there, yield the bound-state energies. The eigenstates will be labeled as $|\tau,j,n\rangle$, with n ordering them in ascending absolute value of the energy.

A similar model was recently studied in Ref. [28],

$$H_\tau = H_0 + \tau\Delta_0\sigma_z + U(r), \tag{8}$$

with a steplike electrostatic, rotationally invariant potential, $U = \Theta(R-r)U_0$ ($U_0 < 0$). Unlike in the case of a MP-QD, Eq. (1), the gap of a PW-QD, Δ_0, is not position dependent, whereas H_0 is again given by Eq. (2). The differences are sketched in the insets of Fig. 1, which outline the spectrum of the two different quantum dots, considered throughout this work.

The relation between the eigenfunctions of Eqs. (1) and (8) is discussed in Appendices A and B, as well as the symmetries they display. Further discussion about the spectra is held in the subsequent sections.

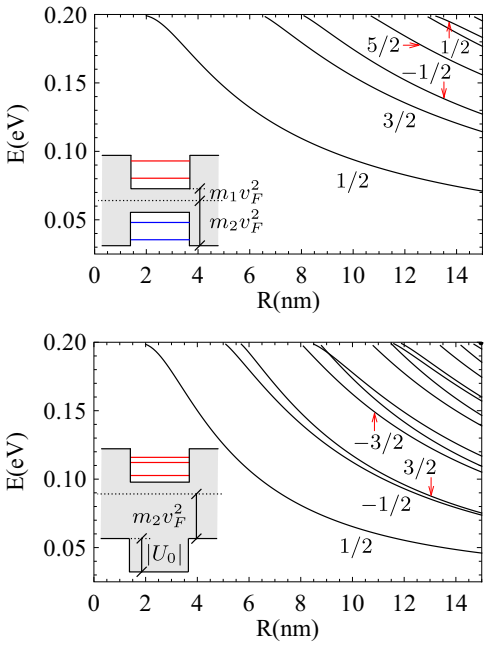

FIG. 1. (Color online) Spectra of a circular MP-QD (upper panel) and a PW-QD (lower panel) for $B = 0$. The values of j respective to $\tau = 1$ label the most bounded energy levels. Insets: Diagrams of the bound-state levels in the mass and potential well. The shadowed region corresponds to forbidden values of the energy, and the colored lines inside the wells represent bound states. The electron- (red) hole (blue) symmetry is only present in the MP-QD.

The mass profile in graphene can be achieved when placing it on an Ir(111) substrate and subsequently covering graphene with Ir or W clusters. Graphene on Ir(111) displays a small gap of ∼50 meV due to the Moiré lattice structure formed by the graphene layer with the substrate, defining a superlattice constant of 2.5 nm. Due to a change in the graphene lattice structure from sp^2 to sp^3 bonding in the covered region [37], this gap is augmented from 50 to 400 meV. In Ref. [33], it was demonstrated that the upper metal clusters of the size of the Moiré superlattice can be removed by an STM tip at will, thus opening up the possibility of creating mass-confined quantum dots of arbitrary size up to nanometer accuracy. Throughout the article, we will therefore use the values found in photoemission spectroscopy experiments [13], i.e., $\Delta_1 = m_1v_F^2 = 0.025$ eV and $\Delta_2 = m_2v_F^2 = 0.2$ eV. In the PW-QD, we choose a confining potential $U_0 = (\Delta_1-\Delta_2)\Theta(r-R)$ which guarantees the the same well depth as in the MP-QD.

III. ELECTRONIC SPECTRUM OF A SINGLE QUANTUM DOT

A. $B = 0$ case

Let us first discuss the spectra in the absence of magnetic fields. Results are plotted in Fig. 1. As is proved in Appendix B, the levels are doubly degenerate,

$$E(\tau,j) = E(-\tau,-j), \tag{9}$$

reflecting the time-reversal symmetry that connects the two valleys. Only for MP-QDs is the electron-hole symmetry also

present,

$$E(\tau, j) = -E(-\tau, j), \tag{10}$$

while it is absent in the case of PW-QDs (cf. also the discussion in Appendix B and the insets of Fig. 1). This aspect implies a striking difference: MP-QDs can host confined electron-hole pairs, whereas they are not present in PW-QDs.

Further comparing the spectra of MP-QDs and PW-QDs, one can notice a higher confinement of the states of the latter. This implies a denser spectrum of PW-QDs for the same depth of the mass and potential well. In turn, the larger level spacing makes MP-QDs more accessible for optical spectroscopy.

For experimentally realizable MP-QDs with $R \lesssim 10$ nm, intraband transitions between bound-state levels have a frequency of the order of 10 THz, enabling our system to support terahertz optical applications. For MP-QDs with $R \lesssim 6$ nm, only one bound state in the conduction band is present, defining a possible qubit which can be optically turned on (electron-hole pair creation) and off (neutral ground state). Furthermore, excitonic effects lifting the valley degeneracy could manifest many-body effects also in the THz range, promoting the system as an experimentally realizable probe for interactions in quantum dots, including electron-phonon coupling [38].

B. $B \neq 0$ case

In Fig. 2, we show the spectra of a MP-QD (upper panel) and a PW-QD (lower panel) as a function of the radius for zero and nonzero magnetic field B. We observe a splitting

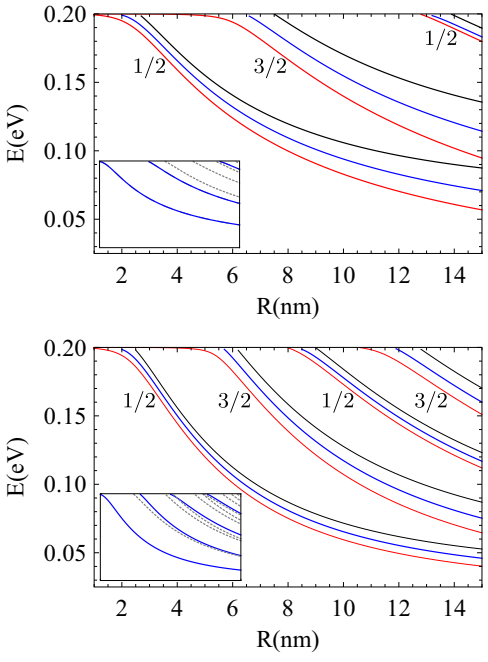

FIG. 2. (Color online) Splitting of the valley degeneracy of a circular MP-QD (upper panel) and a PW-QD (lower panel) when a perpendicular magnetic field is applied. Blue lines correspond to $B = 0$, and they split into black ($\tau = 1$) and red ($\tau = -1$) lines when applying $B = 4$T. For clarity, only levels with $|j| = \{1/2, 3/2\}$ (labels of the curves) have been plotted. In the insets, where the full spectra at $B = 0$ is shown, they are highlighted in blue.

between levels belonging to different ($\tau = \pm 1$) valleys which is proportional to the magnitude of the applied magnetic field. For $B = 4$ T, we can achieve a splitting up to 2 meV (THz regime) for quantum dots with only one bound state (i.e., for $R \lesssim 6$ nm). Remarkably, the splitting of the levels is considerably larger in the MP-QD.

These plots also show that if levels belong to different valleys, their energies are modified by the magnetic field in a different manner. Whereas every $\tau = +1$ level rises with B, some $\tau = -1$ ones are lowered, i.e., become more confined. Interestingly, for some R values for which there were an equal number of $\tau = \pm 1$ states at $B = 0$, we observe that new $\tau = -1$ states appear and other $\tau = +1$ states vanish when applying a sufficiently high magnetic field. The opposite happens in the valence band. As we will see later, this fact will be relevant to explain the spectrum for $R \gg l_B$, with the magnetic length $l_B = \sqrt{\hbar/(eB)}$.

In Fig. 3, we present the spectra as a function of the fixed dot radius R over the magnetic length l_B. They show more clearly one of our previous considerations concerning the appearance and disappearance of states with different valley index, see Fig. 2, i.e., as long as B is increased for a fixed R, some $\tau = +1$ levels are no longer bound states, whereas others with $\tau = -1$ enter the well. Remarkably, one can appreciate three (and not two, as usual) different regions in these plots for both the MP-QD and the PW-QD: (i) for $B \to 0$, we recover the degenerate spectrum, in which the level spacing does not seem to have a definite structure. (ii) As soon as B is sufficiently large, the levels converge to straight lines and to the bottom of the well. (iii) For greater values of B, only bound states with $\tau = -1$ are allowed in the conduction band, see left panels of Fig. 3. In this last case, for energies not close to the top or the bottom of the well, we encounter equally spaced nondegenerate levels. Near the bottom, we can notice how a growing number of states with B converge to the lowest possible energy. We will devote part of this section to discuss the emergence of these patterns featured in points (ii) and (iii).

Concerning the intermediate region (ii), Fig. 3 resembles a typical Fock-Darwin spectrum [20,39] the potential well or the mass profile playing the role of the harmonic potential in that model. In this regime, the energy term corresponding to B dominates over the well depth. This is confirmed by the dependence

$$|E_n| = \sqrt{\Delta^2 + 2n\,(\hbar v_F / l_B)^2} \tag{11}$$

($n \geqslant 0$ refers to the nth asymptote), revealing a structure characteristic of Landau levels in gapped graphene [40,41]. The existence of the lowest Landau level is of particular relevance, since it is responsible for the structure of the spectrum for large B, as discussed below.

The degeneracy of the Landau levels in this region is also noteworthy, which is proportional to the magnetic flux through the system. One can verify this dependence in Fig. 3: While B is increased, more $\tau = -1$ levels appear inside the wells and converge asymptotically to graphene Landau levels, providing them with the required degeneracy.

For B greater than a critical value

$$B_c \simeq \frac{\left(m_2^2 - m_1^2\right) v_F^2}{2e\hbar} \simeq 30 \text{ T}, \tag{12}$$

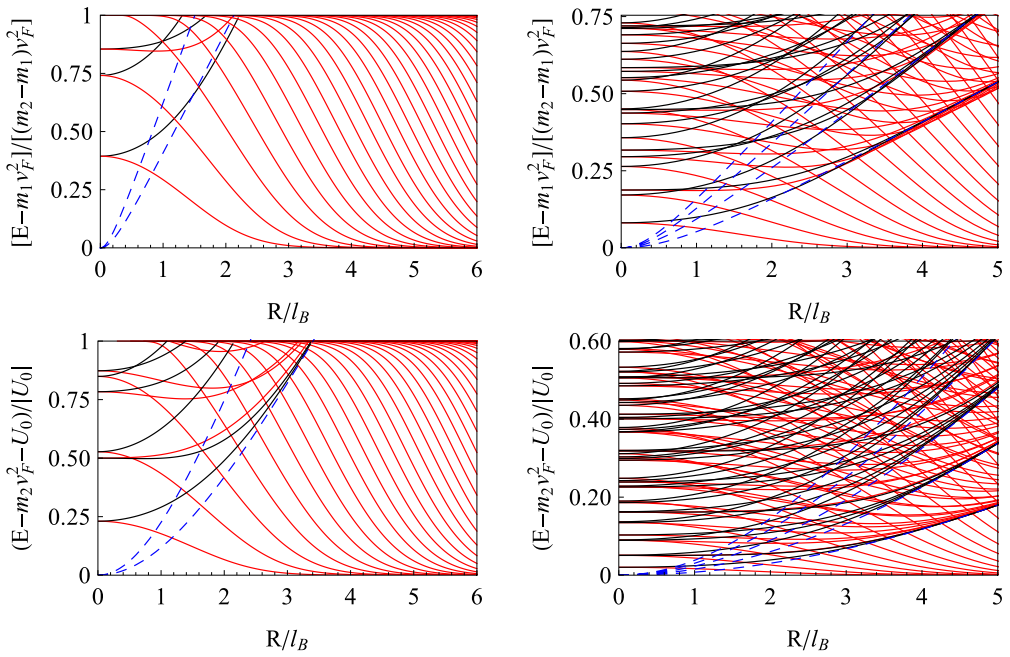

FIG. 3. (Color online) Upper panels: MP-QDs. Lower panels: PW-QDs. Left panels: Spectra for $R = 10$ nm ($R = l_B \Rightarrow B = 6.6$ T). Right panels: Spectra for $R = 40$ nm ($R = l_B \Rightarrow B = 0.41$ T). Black (red) corresponds to $\tau = (-)1$ valley. Convergence to Landau levels (bottom of the well and dashed blue lines) can clearly be appreciated. The spectrum structure with only $\tau = -1$ levels and approximately equidistant energy levels appears for $B > B_c$, see Eq. (12).

only the lowest Landau level will remain, see Fig. 3. We encounter the aforementioned region (iii) with only $\tau = -1$ states. Our previous considerations on the degeneracy explain the level structure of this part of the spectrum. As long as B is increased, a constant income of levels is needed to guarantee that the lowest Landau level is degenerate enough. As a result, our quantum dots show an excited spectrum of equally spaced levels that will converge to the bottom of the well at higher B. Their difference in energy can be tuned with the radius, since a higher area $\mathcal{A}$ increases the degeneracy of Landau levels, in turn implying a greater density of incoming states. Experiments with graphene have been carried out for values of $B \gtrsim B_c$ [42], so this regime may be observable for our values of Δ_1 and Δ_2. As an alternative, pseudomagnetic fields exceeding B_c could be induced by strain [35].

As we have seen, the chiral nature of graphene's carriers manifests itself in the results. The presence of a Landau level whose energy is B independent is the most determinant feature in the quantum dot spectrum. It guarantees the existence of bound states at arbitrarily high values of B with the structure of the third region discussed before. This is in stark contrast to quantum dots of ordinary 2D semiconductors, where no bound states exist beyond some critical B_c. The approximate equidistant level structure might be useful for optical experiments in the THz regime, inducing transitions between several adjacent levels. Since conduction and valence bands host bound states of opposite valleys, no interband transitions are allowed.

IV. ARRAYS OF MP-QDS

The controlled removal of metal clusters on top of graphene placed on an Ir(111) substrate allows for creating artificial periodic lattice structures within the nanoscale [33]. In this section, we will thus focus on linear chains of MP-QDs, setting with this elementary example the proceedure to analyze more complicated one- or two-dimensional arrays. For the sake of simplicity, we fix the dot radius $R = 6.5$ nm, which implies dealing only with a single bound state (cf. Fig. 1) per band. Our aim is to carry out a tight-binding calculation considering both the valence and the conduction band. Later, we will also add the Coulomb interaction between the excitations hosted in different dots.

A. One-particle physics

We start our analysis by considering two MP-QDs whose centers are separated by a distance D. It turns out that the overlap λ of the two wave functions is not negligible for D close to $2R$. This is demonstrated in Fig. 10. Although its square is smaller, we will not neglect it for the moment. Actually, we will show below that its contribution will be relevant for an array of quantum dots with a small lattice parameter $D \simeq 2R$. Henceforth, only $O(\lambda^n)$ terms with $n \geqslant 3$ will be discarded unless the contrary is specified. This introduces an error of less than 1%, see the lower panel of Fig. 5.

A sketch of all different processes that can take place between the two MP-QDs is shown in Fig. 4. In Appendix C, we demonstrate that the probability amplitudes of the hopping processes ξ, κ, μ and $\lambda\kappa$ are relevant, whereas η, the electron-hole annihilation, can be shown to be precisely zero. $\lambda\kappa$ is a term of the order of λ^2 (cf. Fig. 5). It is not a direct hopping parameter like $\{\eta,\kappa,\mu\}$ but a hopping process provoked or *assisted* by the overlap.

The upper panel of Fig. 5 shows the spectrum of the double well as a function of the distance between the centers. There it

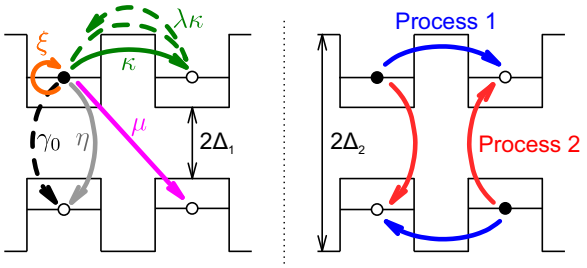

FIG. 4. (Color online) Outline of different hopping processes between two MP-QDs. Left-hand side: Single-particle processes. γ_0 is the spontaneous decay, Eq. (19). Right-hand side: Interaction processes.

can be seen that considering or neglecting terms of the order of the overlap squared does not alter the values of the energies considerably. Nevertheless, the situation will differ in periodic arrays of quantum dots closely packed, as we will discuss below.

In Appendix C, we define a tight-binding model for a linear chain of MP-QDs with $R = 6.5$ nm. The resulting bands appear in Fig. 6, ranging from dispersive to flat with the increase of D. The gaps and carrier effective masses are thus tunable with the lattice parameter.

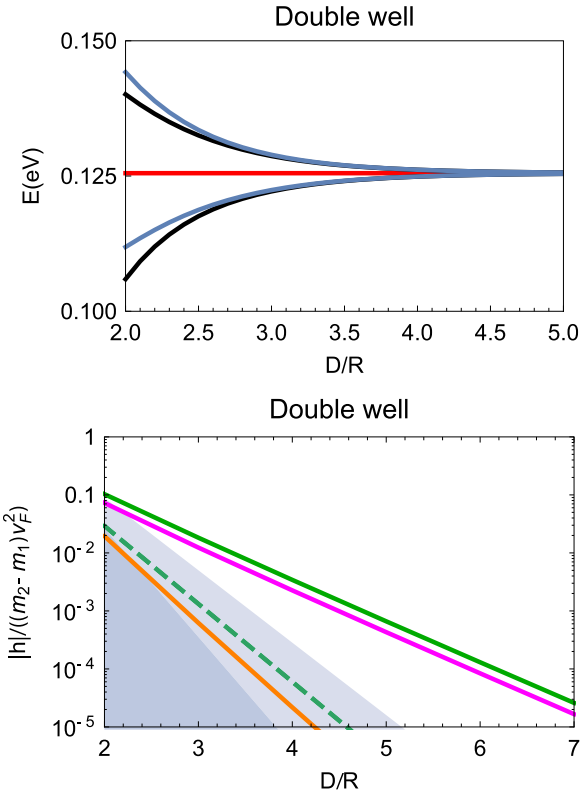

FIG. 5. (Color online) Upper panel: Bound-state energies of two nearby MP-QDs. Red: Bound-state energy of a single well. Black (blue): Bound-state energies neglecting the overlap squared (cubed) of the wave functions. For more details, see Appendix C. Lower panel: Comparison between the hopping processes depicted in Fig. 4 (with the same color code). h labeling the vertical axis refers to κ, μ, and ξ. The strong (light) shadowed region corresponds to values below the overlap cubed (squared).

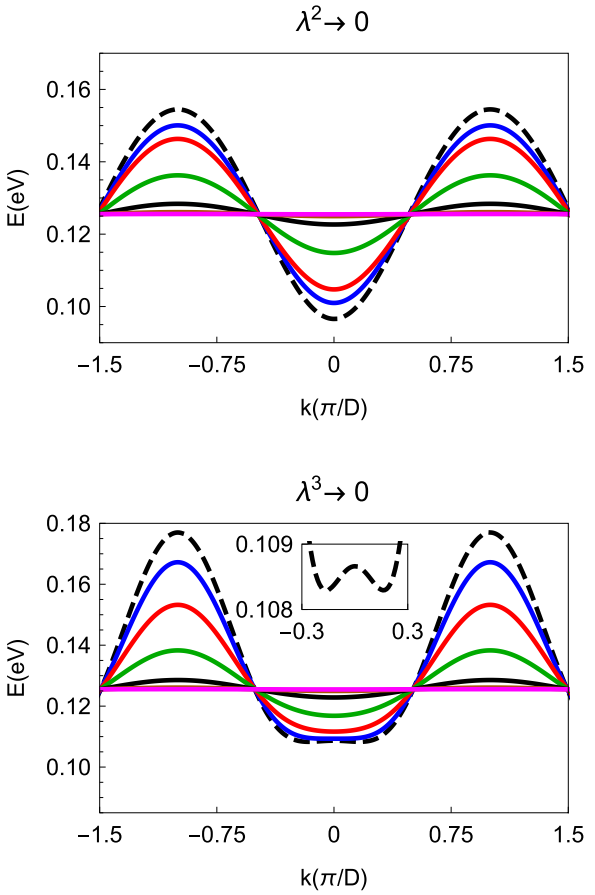

FIG. 6. (Color online) Bands of a one-dimensional chain of quantum dots. From wider to narrower bands, dashed black: $D = 2\,R$; blue: $D = 2.1\,R$; red: $D = 2.3\,R$; green: $D = 2.7\,R$; solid black: $D = 3.5\,R$; orange: $D = 4.5\,R$; magenta: $D = 6\,R$. Terms of higher order than the overlap squared (cubed) are neglected in the upper (lower) panel. The inset plots a close view of the $D = 2\,R$ curve, showing its negative curvature at $k = 0$.

Clearly, for a lattice parameter close to the dot diameter, the effect of the overlap on the band structure is significant. This is mainly due to the next-nearest neighbor hopping assisted by λ, see Fig. 11 and the discussion in Appendix C. Note that this effect cannot take place in a double well and this explains why the influence of the overlap-assisted processes on the eigenenergies was much weaker.

As a result, the effective mass m^* of the carriers with $k \simeq 0$ is strongly renormalized by λ. Remarkably, for a closely packed chain, the overlap-assisted processes give rise to a change of sign in the curvature of the bands around $k = 0$ (see inset of Fig. 6). For low densities, the ground state is thus given by a Fermi ring [43] and shows that the implications of considering second-order processes in a tight-binding approach go beyond a mere correction in eigenenergies.

B. Coulomb interaction

The second part of this section aims to include Coulomb interactions in our system. Processes like those depicted on the right-hand side of Fig. 4 come into play. Their rates γ_C can

be calculated with the help of Fermi's golden rule,

$$\gamma_C = \frac{2\pi}{\hbar}|\langle f|V_{\rm int}|i\rangle|^2 F_{fi}, \tag{13}$$

where $V_{\rm int}$ is the Coulomb interaction and F_{fi} the generalized δ function, see Eq. (15) [44]. $|i\rangle$ ($|f\rangle$) refers to the initial (final) state of the transition which is a two-particle—electron-hole—state,

$$|E\vec{R}_a\rangle \otimes |E'\vec{R}_b\rangle, \tag{14}$$

where, in turn, $|E\vec{R}_\alpha\rangle$ describes the eigenstate with energy E of a single well centered at $\vec{R}_\alpha$. Since we are dealing with only a single bound state per well in the valence and conduction band, and since the Coulomb interaction does not couple valleys nor spins, we can neglect the other quantum numbers (j, τ, spin) that strictly label the state and only keep E and $\vec{R}_\alpha$ in Eq. (14). In the overlap factor

$$F_{fi} = \int_{-\infty}^{\infty} d\epsilon\, \rho_i(\epsilon)\rho_f(\epsilon), \tag{15}$$

a Lorentzian was considered for the density of states of the $|i\rangle$ ($|f\rangle$) level, whose energy is centered at $E_{i(f)}$:

$$\rho_{i(f)}(\epsilon) = \frac{1}{\pi}\frac{\Gamma}{[\epsilon - E_{i(f)}]^2 + \Gamma^2}. \tag{16}$$

A typical broadening of $\Gamma = 10$ meV was used [45].

Process 2 in Fig. 4 is an example of Förster transfer [46]. In this case, one can approximate the matrix element in Eq. (13) by its multipolar expansion,

$$\langle f|V_{\rm int}|i\rangle \simeq \frac{1}{4\pi\epsilon_0}\frac{D\vec{\mu}_a\cdot\vec{\mu}_b - 3(\vec{\mu}_a\cdot\vec{D})(\vec{\mu}_b\cdot\vec{D})}{D^5}, \tag{17}$$

where $\vec{D} = \vec{R}_a - \vec{R}_b$, and in turn $\vec{R}_a$ and $\vec{R}_b$ are the centers of the MP-QDs involved in the process. The dipole momenta are

$$\vec{\mu}_j = \int d^2r\, |\psi(\vec{r} - \vec{R}_j)|^2(\vec{r} - \vec{R}_j), \quad j = \{a,b\}, \tag{18}$$

with $|\psi(\vec{r} - \vec{R}_j)|^2$ the density probability associated to the single-particle bound state centered at $\vec{R}_j$. We checked numerically the excellent agreement between Eq. (17) and the exact value of the transition matrix element.

A comparison between the rates γ of all processes depicted on Fig. 4 is shown in Fig. 7. We highlight the algebraic behavior of the Förster transfer versus the exponential one of all the rest. The spontaneous decay rate [46],

$$\gamma_0 = \frac{\omega_0^3|\vec{\mu}|^2}{3\pi\epsilon_0\hbar c^3} \simeq 1.9\times 10^7\ \mathrm{s}^{-1}, \tag{19}$$

is also plotted as reference, with $\vec{\mu}$ given by Eq. (18) and $\hbar\omega_0$ being the energy difference between the levels involved. For $D \simeq 7R$, this indicates the existence of a regime in which Förster transfer is the dominant process. In that case, the particle-hole excitations have a sufficiently long lifetime to overlap with the adjacent site to form a band. These Frenkel excitons thus can be described by the following quasibosonic tight-binding Hamiltonian in the diluted limit:

$$H \simeq -\sum_{\langle i,j\rangle}\left[t_{\rm ex}a^\dagger(\vec{R}_j)a(\vec{R}_i) + \text{H.c.}\right]. \tag{20}$$

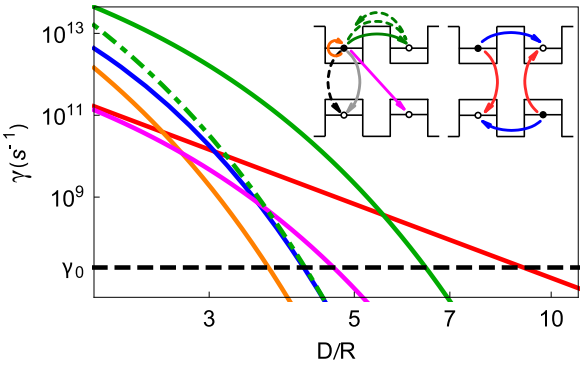

FIG. 7. (Color online) Comparison between the rates γ, Eq. (13), of single-particle and excitonic processes. The color code was introduced in Fig. 4. It is reproduced in the inset for clarity.

Here $a(\vec{R}_i) \equiv c_-^\dagger(\vec{R}_i)c_+(\vec{R}_i)$ annihilates and $a^\dagger(\vec{R}_i) \equiv c_+^\dagger(\vec{R}_i)c_-(\vec{R}_i)$ creates an exciton at lattice site $\vec{R}_i$, where $c_+^{(\dagger)}(\vec{R}_i)$ and $c_-^{(\dagger)}(\vec{R}_i)$ are the electron annihilation (creation) operators in the upper and lower levels of a single dot centered at $\vec{R}_i$, respectively. The excitonic operators $a^{(\dagger)}(\vec{R}_i)$ satisfy bosonic commutation relations in the diluted limit [47].

The effective excitonic hopping amplitude induced by Förster transfer is given by $t_{\rm ex} \equiv \langle +\vec{R}_j; -\vec{R}_i|V_{\rm int}|-\vec{R}_j; +\vec{R}_i\rangle$, which takes place only between nearest neighbors. Other processes, outlined in Appendix C and which were neglected in Eq. (20), would induce a finite lifetime of the excitons. For lattices with $D/R \lesssim 3.5$, the bands turn dispersive (see Fig. 6) and single-particle processes become dominant.

The previous considerations promote the system under study to a highly tunable probe which can further host collective excitations in form of interband plasmons [48,49]. The engineering of lattices exhibiting different symmetries and dimensionality thus opens up a new scenario to explore interactions in artificial lattices.

V. CONCLUSIONS

Motivated by recent experimental advances, we have studied the bound-state spectra of mass-profile quantum dots (MP-QDs) and compared it with the corresponding spectrum of recently studied potential-well quantum dots (PW-QDs). Both systems allow us to confine electrons in 2D and control the lifting of the valley degeneracy by applying a perpendicular magnetic field to the sheet. We have seen that the behavior of their spectra as a function of the radius and the magnetic field is similar, but the level structure of MP-QDs is somehow simpler. This could make the latter more suitable for optical applications in the midinfrared and THz regime. Moreover, we have featured different regions of the spectra according to the magnitude of the magnetic field. Besides the quantum dot spectrum at $B \to 0$, we have discussed the convergence to Landau levels at intermediate values of B and the appearance of an equally spaced level structure for large B fields. The latter arises due to the existence of a lowest Landau level pinned to the band edge whose energy is B independent, in stark contrast with quantum dots hosted by conventional 2D systems.

In the second part, the electronic spectrum of linear chains of MP-QDs with fixed radius $R = 6.5\,\text{nm}$ (and therefore a single valence and conduction bound level) was discussed. Bands of tunable gap and curvature were then obtained. Overlap-assisted processes are shown to play a significant role for closely packed arrays, renormalizing the effective mass of the carriers to the extent of changing its sign for $D \simeq 2R$. When including interactions, the engineered lattice parameter allows us to encounter Frenkel excitons. Remarkably, a system of bosons in a linear chain ultimately governed by efficient Förster transfer between adjacent dots can be reproduced for $D \simeq 7R$. Further research on the possibility of hosting Bose-Einstein condensates in this kind of systems remains to be explored in future works.

ACKNOWLEDGMENTS

We thank H. Ochoa, B. Amorim, F. Marchetti, I. Brihuega, and F. Guinea for useful discussions. This work was supported by the Spanish ministry MINECO under Grant No. FIS2013-44098-P.

APPENDIX A: WAVE FUNCTIONS OF THE BOUND STATES FOR $B \neq 0$

In this appendix, we present the general formulas necessary to solve the eigenvalue problem of a MP-QD. The general solution of Eq. (5) is given by

$$\chi_\sigma^\tau(r) = e^{-br^2/2} r^{n_\sigma} \begin{cases} \alpha_\sigma M[q_\sigma(m_1), 1+n_\sigma, br^2] & \text{for } r \leqslant R, \\ \beta_\sigma U[q_\sigma(m_2), 1+n_\sigma, br^2] & \text{for } r > R, \end{cases} \tag{A1}$$

with

$$q_\sigma(m) = \frac{1}{4}\left[\frac{a_\sigma}{b} + 2(1+n_\sigma)\right] \tag{A2}$$

and Eqs. (6) and (7). U and M are the confluent hypergeometric functions [50]. Since the wave function has to be nonsingular at the origin and square integrable, U (M) can only be a solution in the region $r > R$ ($r \leqslant R$). The ratio $\alpha_\sigma/\beta_\sigma$ is provided by the coupled equations resulting from inserting Eq. (4) in Eq. (1).

When imposing the continuity of the wave function at the frontier $r = R$ [51,52], the following conditions are obtained:

$$j > 0 \Rightarrow \frac{U(q_1(m_2), 1+n_1, bR^2)}{M(q_1(m_1), 1+n_1, bR^2)} = \frac{\tau E + \Delta(m_1)}{[\tau E + \Delta(m_2)]\left[1 - \frac{q_1(m_1)}{1+n_1}\right]} \frac{U(q_{-1}(m_2), 1+n_{-1}, bR^2)}{M(q_{-1}(m_1), 1+n_{-1}, bR^2)}, \tag{A3}$$

$$j < 0 \Rightarrow \frac{U(q_{-1}(m_2), 1+n_{-1}, bR^2)}{M(q_{-1}(m_1), 1+n_{-1}, bR^2)} = -\frac{(1+n_{-1})q_{-1}(m_2)[\tau E - \Delta(m_1)]}{q_{-1}(m_1)[\tau E - \Delta(m_2)]} \frac{U(q_1(m_2), 1+n_1, bR^2)}{M(q_1(m_1), 1+n_1, bR^2)}. \tag{A4}$$

They yield the allowed energies of the bound states.

It is possible to relate the solution of Eq. (5) (MP-QDs) and Eq. (8) (PW-QDs). The substitution

$$E \to E - U(r), \quad \Delta \to \Delta_0, \quad m_1 \to m_2, \tag{A5}$$

in Eq. (A1) provides the wave functions of Eq. (8). The matching conditions then yield Eqs. (A3) and (A4) but with the changes

$$\tau E \pm \Delta(m_1) \to \tau(E - U_0) \pm \Delta_0, \tag{A6}$$

$$\tau E \pm \Delta(m_2) \to \tau E \pm \Delta_0. \tag{A7}$$

Moreover, in Eq. (6) when inserted in Eq. (A2), $E \to E - U_0$ for $q_\sigma(m_1)$, whereas $E \to E$ for $q_\sigma(m_2)$. The whole set of substitutions can be understood under the following consideration: Focusing on Eqs. (A3) and (A4), the different masses m_1 and m_2 only appear for the regions $r \leqslant R$ and $r > R$, respectively. In order to obtain the solution of a PW-QD, we thus change $E \to E - U_0$ only in the case $r \leqslant R$. On the other hand, $m_1 \to m_2$, i.e., $\Delta(r) \to \Delta_0$, holds everywhere.

The electron-hole symmetry of the solution for MP-QDs can be inferred directly from Eqs. (A3) and (A4). They depend on the energy solely through the variable τE. Therefore, given a state with (E, τ, j), another with $(-E, -\tau, j)$ exists. Nevertheless, this symmetry is broken in PW-QDs. The reason is that the substitutions given by Eqs. (A6) and (A7) in Eqs. (A3) and (A4) split the dependence on τE in τ and E separately.

Plots of the wave-function components appear in Fig. 8. In the upper panels, the effect of increasing the magnetic field is analyzed. A polarization of the B sublattice takes place in both valleys and the quenching of the kinetic energy with magnetic field is revealed as a shift of the radial probability towards the center of the well. The lower panels, on the other hand, focus on levels with different j values at a fixed B field. The increase in the total angular momentum J_z entails a shift of the radial probability away from the center of the dot. This is in agreement with the lower localization of the states with energies closer to the top of the well.

APPENDIX B: WAVE FUNCTIONS OF THE BOUND STATES FOR $B = 0$

In the case of $B = 0$, Eq. (A1) reduces to

$$\chi_\sigma^\tau(r) = \begin{cases} \delta_\sigma J_{j-\sigma/2}[k(m_1)r] & \text{for } r \leqslant R, \\ \gamma_\sigma H^{(1)}_{j-\sigma/2}[i\,k(m_2)r] & \text{for } r > R. \end{cases} \tag{B1}$$

In turn,

$$k(m) \equiv \sqrt{\left|\left(\tau E - mv_F^2\right)\left(\tau E + mv_F^2\right)\right|}/\hbar v_F \tag{B2}$$

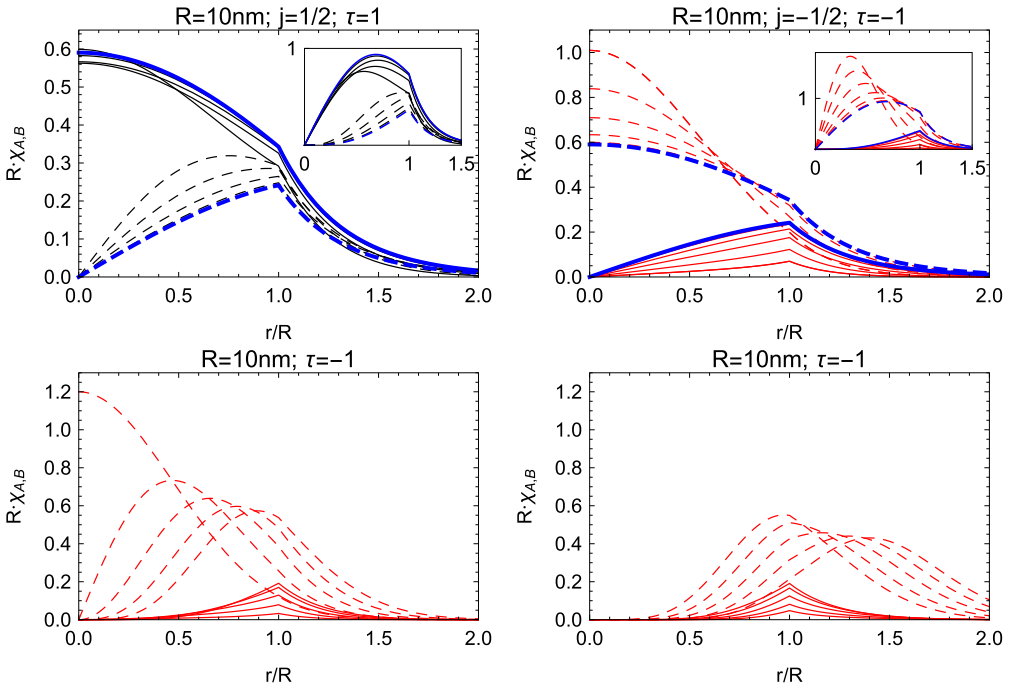

FIG. 8. (Color online) Components of the MP-QD wave function, Eqs. (A1) and (4). Solid (dashed) lines refer to the A (B) sublattice. Upper panels: Plots for different values of the magnetic field B. The thick blue curves correspond to zero magnetic field ($B = 0$), whereas black ($\tau = 1$) and red ($\tau = -1$) curves show the eigenfunctions at finite magnetic field for $R/l_B = \{1, 1.5, 2\}$: Greater values of R/l_B are respective to the more deviated curves from the blue ones. For comparison, an extra solution for $R/l_B = 2.5$ in the regime with only $\tau = -1$ levels has been plotted for $\tau = -1$. The insets depict the radial probability ($2\pi r R|\chi_{A,B}|^2$ vs r/R) associated to the wave functions. Lower panels: Plots for $R = 10\,\text{nm}$, $R/l_B = 3$, corresponding to the region where only $\tau = -1$ levels are present and different values of j. Left plot: $j = \{-1/2, -3/2, -5/2, -7/2, -9/2\}$ corresponding to A (B) sublattice curves ordered from bottom (left) to top (right). Right plot: $j = \{-11/2, -13/2, -15/2, -17/2, -19/2\}$ corresponding to A (B) sublattice curves ordered from top (left) to bottom (right).

and $J_{j-\sigma/2}$ and $H^{(1)}_{j-\sigma/2}$ are the Bessel functions and the Hankel functions of the first kind as defined in Ref. [50]. The ratio $\delta_\sigma/\gamma_\sigma$ is calculated analogously to $\alpha_\sigma/\beta_\sigma$ in Appendix A.

The continuity condition for the wave function yields in this case

$$i\,\tau\,\mathrm{sg}(E)\eta(m_2)J_{j-1/2}\left[k(m_1)R\right]H^{(1)}_{j+1/2}\left[i\,k(m_2)R\right] = \eta(m_1)J_{j+1/2}\left[k(m_1)R\right]H^{(1)}_{j-1/2}\left[i\,k(m_2)R\right], \quad \text{(B3)}$$

which again gives the allowed energies of the bound states. We also defined

$$\eta(m) \equiv \sqrt{\left|\frac{\tau E - m v_F^2}{\tau E + m v_F^2}\right|}. \quad \text{(B4)}$$

The considerations regarding the electron-hole symmetry which are related to the τE dependence also apply here, see Appendix A. Moreover, the properties of Bessel and Hankel

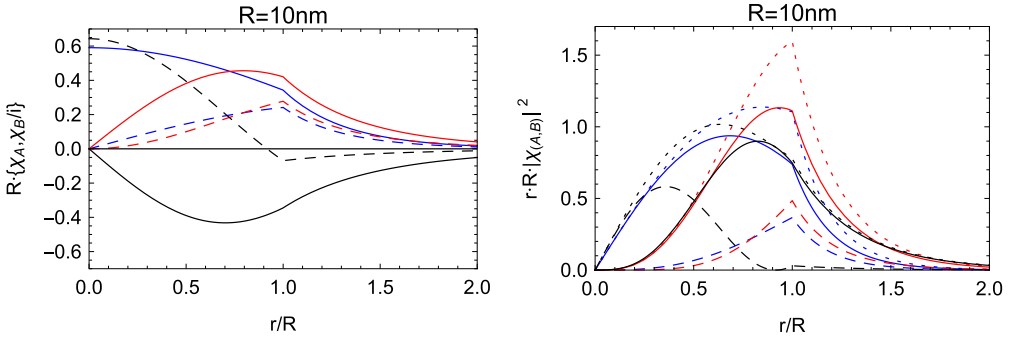

FIG. 9. (Color online) Components of the wave function (left-hand side), Eqs. (B1) and (4), and their associated radial probabilities (right-hand side) for $\tau = 1$ and $j = 1/2$ [blue (dark gray)], $j = 3/2$ (red), and $j = -1/2$ (black). Solid (dashed) lines correspond to the A (B) sublattice and dotted lines to the total radial density probability. A wave function with $\tau = -1$ and $j = -1/2$ is also plotted in Fig. 8 (right-hand side of upper panel).

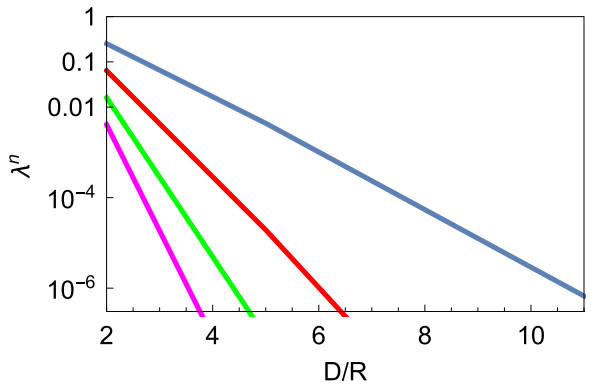

FIG. 10. (Color online) Overlap between wave functions belonging to wells whose centers lie at a distance D. $n = 1,2,3,4$ correspond, from top to bottom, to blue, red, green, and magenta.

functions

$$J_{-n}(z) = (-1)^n J_n, \quad H^{(1)}_{-\nu}(z) = e^{\nu\pi i} H^{(1)}_{\nu}(z), \tag{B5}$$

together with

$$\frac{\eta(m_1)}{\eta(m_2)} \xrightarrow{\tau\to-\tau} \frac{\eta(m_2)}{\eta(m_1)}, \tag{B6}$$

allow us to prove the double degeneracy of levels, i.e., a solution with (E,τ,j) implies the existence of another with $(E,-\tau,-j)$. In contrast with the electron-hole symmetry, the substitutions of Eqs. (A6) and (A7) in Eq. (B3) (yielding a PW-QD) do not lift this degeneracy. As we mention in the main text and show in Figs. 2 and 3, a splitting happens when a magnetic field is applied. Plots of several wave functions and their corresponding radial probabilities are shown in Fig. 9.

APPENDIX C: TIGHT BINDING IN A LATTICE OF MP-QDS

Our aim is to construct a tight-binding model for a system in which the overlap λ of neighboring wave functions cannot be neglected. This is motivated by Fig. 10, which plots the overlap for a couple of quantum dots as a function of the distance. As a starting point, we will discard terms which are cubic or of higher order in λ. Actually, we will show that $O(\lambda^2)$ terms will be significant in packed lattices of quantum dots.

Let $|n\rangle$ be the wave function of a particular state of a single well located at a certain position. The set S containing all $|n\rangle$ kets respective to every lattice site and every energy level is not orthonormal because the overlap $\langle n|n'\rangle$ between neighbors is not negligible. However, the Gram-Schmidt algorithm allows us to obtain an orthonormal basis S' by linear combinations of the vectors belonging to S. Denoting the elements of S' by $|f_n\rangle$, we can write the identity as

$$I = \sum_n |f_n\rangle\langle f_n|. \tag{C1}$$

Carrying out the algorithm to obtain $|f_n\rangle$, the unity operator in terms of the S-basis vectors only, including correction terms to lowest orders, reads

$$I = \sum_n |n\rangle\langle n| - \sum_{j\neq n} \langle j|n\rangle |j\rangle\langle n|. \tag{C2}$$

To express the Hamiltonian in the original basis S, we will use this representation of the identity operator.

Let us apply the aforementioned procedure to a set of N MP-QDs whose centers are located at $\vec{R}_i$ with $i = \{1,\ldots,N\}$. We will consider wells that only have one valence and conduction bound state with energy $\pm E$ ($E > 0$) and $j = \pm 1/2$ (cf. Fig. 1). Therefore, we can univocally label the S states by $|\pm\vec{R}_i\rangle$.

We define the following parameters, describing the hopping processes depicted in Fig. 4:

$$\lambda^{\pm}_{ij} = \langle \pm\vec{R}_i|\pm\vec{R}_j\rangle, \tag{C3}$$

$$\xi^{\pm} = \langle \pm\vec{R}_i|\Delta U_i|\pm\vec{R}_i\rangle, \tag{C4}$$

$$\eta^{\pm} = \langle \pm\vec{R}_i|\Delta U_i|\mp\vec{R}_i\rangle, \tag{C5}$$

$$\kappa^{\pm}_{ij} = \langle \pm\vec{R}_i|\Delta U_j|\pm\vec{R}_j\rangle, \tag{C6}$$

$$\mu^{\pm}_{ij} = \langle \pm\vec{R}_i|\Delta U_j|\mp\vec{R}_j\rangle. \tag{C7}$$

Assuming inversion symmetry for the array under consideration and making use of the properties of the wave functions, the following identities can be proved:

$$\{\lambda^{\pm}_{ij},\xi^{\pm},\kappa^{\pm}_{ij}\} \in \mathbb{R}, \quad \lambda^{+}_{ij} = \lambda^{-}_{ij} \equiv \lambda_{ij}, \quad \lambda_{ij} = \lambda_{ji}, \tag{C8}$$

$$\xi^{+} = -\xi^{-}, \quad \eta^{\pm} = 0, \quad \kappa^{+}_{ij} = -\kappa^{-}_{ij}, \quad \kappa^{\pm}_{ij} = \kappa^{\pm}_{ji}, \tag{C9}$$

$$\mu^{\pm}_{ij} \equiv \mu^{\pm}(\vec{R}_i - \vec{R}_j) = \mu^{\pm}(|\vec{R}_j - \vec{R}_i|\hat{x})e^{\pm i\theta_{\vec{R}_j-\vec{R}_i}}, \tag{C10}$$

$$\mu^{\pm}(|\vec{R}_j - \vec{R}_i|\hat{x}) \in \mathbb{R}, \quad \mu^{+}_{ij} = -\mu^{-*}_{ij}. \tag{C11}$$

$\hat{x}$ is the unitary vector in the x direction, $\theta_{\vec{R}_j-\vec{R}_i}$ is the angle between $\vec{R}_j - \vec{R}_i$, and $\hat{x}$ and $h(\vec{R}_i - \vec{R}_j) \equiv h_{ij}$, where $h = \{\lambda^{\pm},\kappa^{\pm},\mu^{\pm}\}$. In turn,

$$\Delta U_j = H - H_{\vec{R}_j}, \tag{C12}$$

$H = \sum_i H_{\vec{R}_i}$ being the total Hamiltonian and $H_{\vec{R}_j}$ the Hamiltonian of a single MP-QD centered at $\vec{R}_j$. ΔU_j accounts then for the influence of the lattice on the Hamiltonian of an isolated dot and results in the hopping of electrons between different wells.

The dependence of Eqs. (C3)–(C7) on D/R, where D is the distance between the centers of the dots, is plotted in Fig. 5 for a double MP-QD. It can be seen that $\{\mu,\kappa\} < \lambda(m_2 - m_1)v_F^2$ and $\xi < \lambda^2(m_2 - m_1)v_F^2$, which will be taken into account when discarding terms of greater order than λ^2 in subsequent calculations.

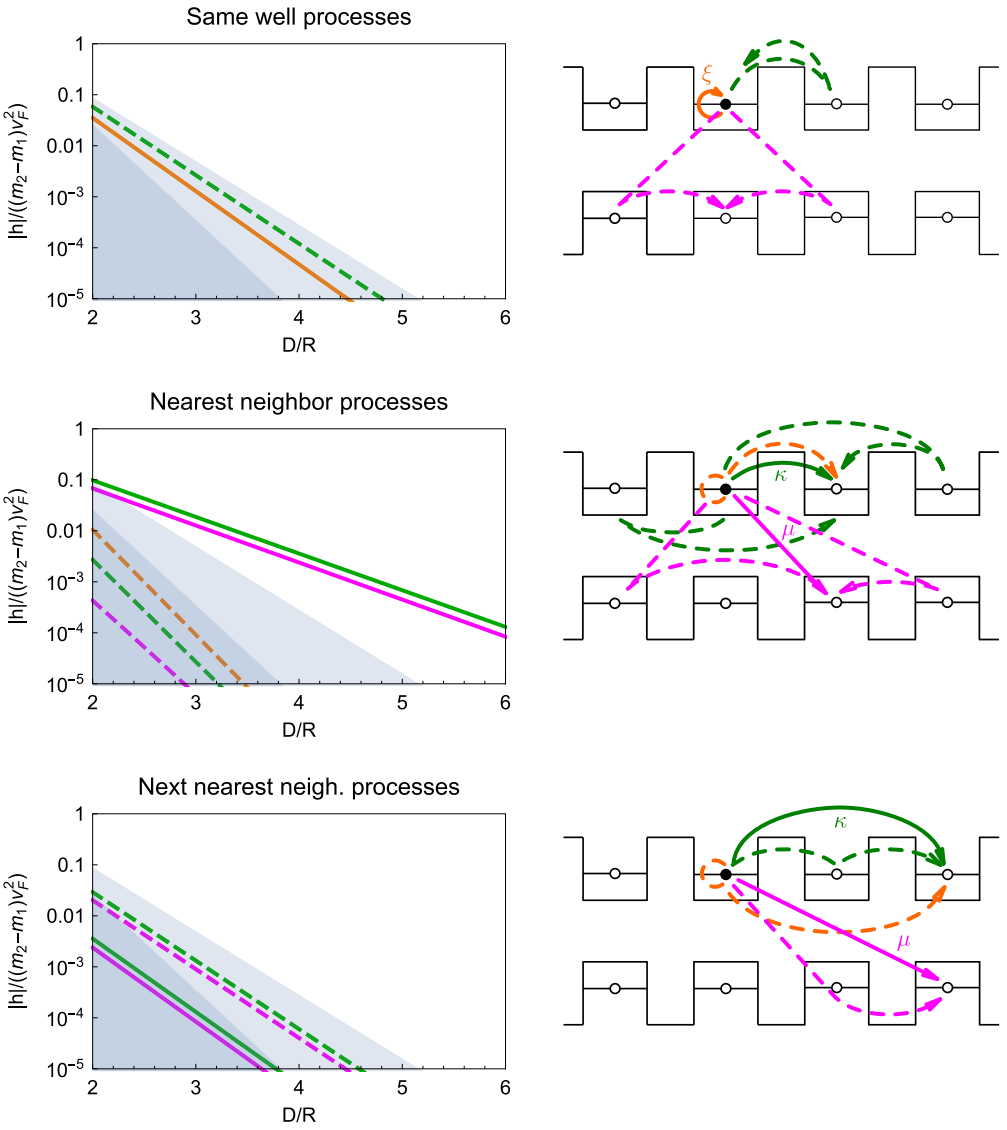

FIG. 11. (Color online) Analogous to Fig. 5. Hopping processes to the same well, to a nearest neighbor, or to a next-nearest neighbor are analyzed separately. The sketches on the right give the legend of the plots on the left. Solid lines correspond to direct processes, and dashed lines to processes assisted by λ together with a direct hopping, i.e., terms of the kind $\sum_{i,j,m}\lambda_{ji}h^{\pm}_{im}$ appearing in Eq. (C13) ($h=\{\xi,\kappa,\mu\}$). When in each right outline several processes are labeled by a single linestyle, the associated curve on the left plot corresponds to the sum of their probability amplitudes. In the upper left plot, the magenta processes do not appear because the sum of their amplitudes vanishes due to Eq. (C10). In the bottom left plot, the amplitude of the orange process is not identically zero but so small that lies outside the plot range. For shadowed regions, see Fig. 5.

Under these considerations and with Eq. (C2), the Hamiltonian acting on $|\pm\vec{R}_m\rangle$ can be expressed as

$$H|\pm\vec{R}_m\rangle=\left(H_{\vec{R}_m}+I\cdot\Delta U_m\right)|\pm\vec{R}_m\rangle=\left[\pm|E|+\xi^{\pm}-\sum_{i\neq m}\lambda_{mi}\kappa^{\pm}_{im}\right]|\pm\vec{R}_m\rangle$$
$$+\sum_{j\neq m}\left[\kappa^{\pm}_{jm}-\xi^{\pm}\lambda_{jm}-\sum_{i\neq\{j,m\}}\lambda_{ji}\kappa^{\pm}_{im}\right]|\pm\vec{R}_j\rangle+\sum_{j\neq m}\left[\mu^{\pm}_{jm}-\sum_{i\neq\{j,m\}}\lambda_{ji}\mu^{\pm}_{im}\right]|\mp\vec{R}_j\rangle-\sum_{j\neq m}\lambda_{mj}\mu^{\pm}_{jm}|\mp\vec{R}_m\rangle. \tag{C13}$$

Equation (C13) gives the matrix elements of H in the S basis for a still unspecified geometry of the quantum dot set. This general result can be applied to different systems. The simplest consists in only two coupled MP-QDs. Its spectrum, with the individual energy levels split, appears in Fig. 5. One can see there that for $D\lesssim 4R$, the influence of $O(\lambda)$ terms

is significant, although there is not a great difference between neglecting λ^2 and λ^3 terms even at small distances between the wells. Second-order processes, however, will be more relevant in lattices due to the assistance of next-nearest-neighbor hopping processes, see the following discussion and Fig. 11.

For a periodic system of MP-QDs, it is more convenient to work in a Fourier-transformed basis defined by

$$|\pm\vec{R}\rangle = \frac{1}{2\pi}\int d^2k\, e^{i\vec{k}\cdot\vec{R}}|\pm\vec{k}\rangle. \tag{C14}$$

Inserting Eq. (C14) into Eq. (C13), the Hamiltonian can be expressed in block diagonal form. The block respective to $\vec{k}$ reads

$$H(\vec{k}) \equiv \begin{bmatrix} \langle -\vec{k}|H|-\vec{k}\rangle & \langle -\vec{k}|H|+\vec{k}\rangle \\ \langle +\vec{k}|H|-\vec{k}\rangle & \langle +\vec{k}|H|+\vec{k}\rangle \end{bmatrix} = \begin{bmatrix} h_1^- + \sum_{\vec{\delta}} h_{2,\vec{\delta}}^- e^{i\vec{k}\cdot\vec{\delta}} & \sum_{\vec{\delta}} h_{3,\vec{\delta}}^- e^{i\vec{k}\cdot\vec{\delta}} \\ \sum_{\vec{\delta}} h_{3,\vec{\delta}}^+ e^{i\vec{k}\cdot\vec{\delta}} & h_1^+ + \sum_{\vec{\delta}} h_{2,\vec{\delta}}^+ e^{i\vec{k}\cdot\vec{\delta}} \end{bmatrix}. \tag{C15}$$

Dropping the subindicies, $\vec{\delta}$ is defined by

$$\vec{\delta} = \vec{R}_j - \vec{R}_m, \tag{C16}$$

choosing the adequate j and m. We have also defined, correspondingly,

$$h_1^{\pm} = \pm|E| + \xi^{\pm} - \sum_{i\neq m}\lambda_{mi}\kappa_{im}^{\pm}, \tag{C17}$$

$$h_{2,\vec{\delta}}^{\pm} = \kappa_{jm}^{\pm} - \xi^{\pm}\lambda_{jm} - \sum_{i\neq\{j,m\}}\lambda_{ji}\kappa_{im}^{\pm}, \tag{C18}$$

$$h_{3,\vec{\delta}}^{\pm} = \mu_{jm}^{\pm} - \sum_{i\neq m}\lambda_{ji}\mu_{im}^{\pm}. \tag{C19}$$

The following identities, the last of which guarantees the hermiticity of the Hamiltonian, can be proved attending to the symmetry of the wave functions and ΔU_j:

$$h_1^+ = -h_1^-; \quad h_{2,\vec{\delta}}^+ = -h_{2,\vec{\delta}}^-; \quad h_{3,\vec{\delta}}^+ = h_{3,-\vec{\delta}}^{-\,*}. \tag{C20}$$

We can apply the general result Eq. (C15) to the simplest lattice, namely a one-dimensional chain with a single atom per node. To do so, we must determine the relevant processes which contribute significantly to Eqs. (C17)–(C19). That analysis was carried out and is summarized in Fig. 11.

There we see that departing from the criterium of neglecting λ^2, only the direct processes κ and μ between neighboring wells are relevant. However, as long as the chain lattice parameter becomes close to the diameter of the wells, $O(\lambda^2)$ processes become increasingly more relevant. In particular, a next-nearest-neighbor (nnn) hopping process is assisted by the wave function overlap, whereas direct processes to nnn are negligible.

Once we have discarded all irrelevant terms in Eqs. (C17)–(C19), we can diagonalize Eq. (C15) to obtain the bands and the tight-binding description is complete. Spectra for various lattice parameters are plotted in Fig. 6.

[1] M. I. Katsnelson, K. S. Novoselov, and A. K. Geim, Nat. Phys. **2**, 620 (2006).
[2] A. H. Castro Neto, F. Guinea, N. M. R. Peres, K. S. Novoselov, and A. K. Geim, Rev. Mod. Phys. **81**, 109 (2009).
[3] L. A. Ponomarenko, F. Schedin, M. I. Katsnelson, R. Yang, E. W. Hill, K. S. Novoselov, and A. K. Geim, Science **320**, 356 (2008).
[4] C. Volk, C. Neumann, S. Kazarski, S. Fringes, S. Engels, F. Haupt, A. Müller, and C. Stampfer, Nat. Commun. **4**, 1753 (2013).
[5] C. Stampfer, J. Güttinger, S. Hellmüller, F. Molitor, K. Ensslin, and T. Ihn, Phys. Rev. Lett. **102**, 056403 (2009).
[6] J. Baringhaus, M. Ruan, F. Edler, A. Tejeda, M. Sicot, A. Taleb-Ibrahimi, A.-P. Li, Z. Jiang, E. H. Conrad, C. Berger *et al.*, Nature **506**, 349 (2014).
[7] P. Recher, B. Trauzettel, A. Rycerz, Y. M. Blanter, C. W. J. Beenakker, and A. Morpurgo, Phys. Rev. B **76**, 235404 (2007).
[8] B. Wunsch, T. Stauber, and F. Guinea, Phys. Rev. B **77**, 035316 (2008).
[9] I. Romanovsky, C. Yannouleas, and U. Landman, Phys. Rev. B **87**, 165431 (2013).
[10] P. G. Silvestrov and K. B. Efetov, Phys. Rev. Lett. **98**, 016802 (2007).
[11] A. De Martino, L. Dell'Anna, and R. Egger, Phys. Rev. Lett. **98**, 066802 (2007).
[12] N. Peres, J. Rodrigues, T. Stauber, and J. L. dos Santos, J. Phys. Condensed Matter **21**, 344202 (2009).
[13] S. Rusponi, M. Papagno, P. Moras, S. Vlaic, M. Etzkorn, P. M. Sheverdyaeva, D. Pacilé, H. Brune, and C. Carbone, Phys. Rev. Lett. **105**, 246803 (2010).
[14] B. Hunt, J. Sanchez-Yamagishi, A. Young, M. Yankowitz, B. J. LeRoy, K. Watanabe, T. Taniguchi, P. Moon, M. Koshino, P. Jarillo-Herrero *et al.*, Science **340**, 1427 (2013).
[15] M. S. Fuhrer, Science **340**, 1413 (2013).
[16] J. R. Lima, Phys. Lett. A **379**, 179 (2015).
[17] G. M. Maksimova, E. S. Azarova, A. V. Telezhnikov, and V. A. Burdov, Phys. Rev. B **86**, 205422 (2012).
[18] W. Liu, Z. F. Wang, Q. W. Shi, J. Yang, and F. Liu, Phys. Rev. B **80**, 233405 (2009).
[19] R. Jackiw, Phys. Scripta **2012**, 014005 (2012).
[20] G. J. Ferreira and D. Loss, Phys. Rev. Lett. **111**, 106802 (2013).
[21] M. Z. Hasan and C. L. Kane, Rev. Mod. Phys. **82**, 3045 (2010).
[22] X.-L. Qi and S.-C. Zhang, Rev. Mod. Phys. **83**, 1057 (2011).
[23] D. Loss and D. P. DiVincenzo, Phys. Rev. A **57**, 120 (1998).
[24] B. Trauzettel, D. V. Bulaev, D. Loss, and G. Burkard, Nat. Phys. **3**, 192 (2007).
[25] A. Rycerz, J. Tworzydło, and C. Beenakker, Nat. Phys. **3**, 172 (2007).
[26] J. Güttinger, T. Frey, C. Stampfer, T. Ihn, and K. Ensslin, Phys. Rev. Lett. **105**, 116801 (2010).
[27] N. Rohling, M. Russ, and G. Burkard, Phys. Rev. Lett. **113**, 176801 (2014).
[28] P. Recher, J. Nilsson, G. Burkard, and B. Trauzettel, Phys. Rev. B **79**, 085407 (2009).

[29] M. V. Berry and R. J. Mondragon, Proc. R. Soc. Lond. A **412**, 53 (1987).
[30] G. Giavaras and F. Nori, Appl. Phys. Lett. **97**, 243106 (2010).
[31] G. Giavaras and F. Nori, Phys. Rev. B **83**, 165427 (2011).
[32] J.-L. Zhu, X. Wang, and N. Yang, Phys. Rev. B **86**, 125435 (2012).
[33] A. J. Martínez-Galera, I. Brihuega, A. Gutiérrez-Rubio, T. Stauber, and J. M. Gómez-Rodríguez, Sci. Rep. **4**, 7314 (2014).
[34] P. Recher and B. Trauzettel, Nanotechnology **21**, 302001 (2010).
[35] N. Levy, S. Burke, K. Meaker, M. Panlasigui, A. Zettl, F. Guinea, A. C. Neto, and M. Crommie, Science **329**, 544 (2010).
[36] Z. F. Wang and F. Liu, Nanoscale **3**, 4201 (2011).
[37] P. J. Feibelman, Phys. Rev. B **77**, 165419 (2008).
[38] T. Stauber and R. Zimmermann, Phys. Rev. B **73**, 115303 (2006).
[39] G. Giuliani and G. Vignale, *Quantum Theory of the Electron Liquid* (Cambridge University Press, Cambridge, UK, 2005).
[40] F. D. M. Haldane, Phys. Rev. Lett. **61**, 2015 (1988).
[41] M. Koshino and T. Ando, Phys. Rev. B **81**, 195431 (2010).
[42] P. Plochocka, C. Faugeras, M. Orlita, M. L. Sadowski, G. Martinez, M. Potemski, M. O. Goerbig, J.-N. Fuchs, C. Berger, and W. A. de Heer, Phys. Rev. Lett. **100**, 087401 (2008).
[43] T. Stauber, N. M. R. Peres, F. Guinea, and A. H. Castro Neto, Phys. Rev. B **75**, 115425 (2007).
[44] A. O. Govorov, Phys. Rev. B **68**, 075315 (2003).
[45] K. F. Mak, M. Y. Sfeir, Y. Wu, C. H. Lui, J. A. Misewich, and T. F. Heinz, Phys. Rev. Lett. **101**, 196405 (2008).
[46] L. Novotny and B. Hecht, *Principles of Nano-optics* (Cambridge University Press, Cambridge, UK, 2012).
[47] J. Sólyom, *Fundamentals of the Physics of Solids: Normal, Broken-Symmetry, and Correlated Systems*, Vol. 3 (Springer, Berlin, 2010).
[48] T. Stauber, J. Phys.: Condensed Matter **26**, 123201 (2014).
[49] T. Langer, D. Förster, C. Busse, T. Michely, H. Pfnür, and C. Tegenkamp, New J. Phys. **13**, 053006 (2011).
[50] M. Abramowitz and I. A. Stegun, *Handbook of Mathematical Functions* (Courier Corporation, 1964).
[51] V. Alonso, S. D. Vincenzo, and L. Mondino, Eur. J. Phys. **18**, 315 (1997).
[52] E. McCann and V. I. Fal'ko, J. Phys.: Condensed Matter **16**, 2371 (2004).